Supplementary Note

1. Methods

Preparation of IP samples for mass spectrometry analyses

A fraction of the IP underwent Filter Aided Sample Preparation (FASP) according to the procedure described by Wisniewski *et al.*[1]. The samples were reduced by adding DTT to a final concentration of ~83.3 mM, incubated for 5 min at 99°C and cooled to room temperature. 4× volume of 8 M urea in 100 mM Tris-HCl pH 8.5 (UA) was added to the sample, mixed and stepwise added to a UA-washed Microcon-30 kDa filter (Millipore, MRCF0R030). The filters were then washed with 200 µl UA to wash out residual SDS. The proteins were alkylated with 100 µl of 50 mM iodoacetamide in the dark for 30 min at RT. Afterwards, three washing steps with 100 µl of UA solution were performed, followed by three washing steps with 100 µl of 50 mM TEAB buffer. Proteins were digested with trypsin (Promega, V511X) overnight at 37°C. Peptides were recovered using 40 µl of 50 mM TEAB buffer followed by 50 µl of 0.5 M NaCl. Peptides were desalted using C18 solid phase extraction spin columns (The Nest Group, SEM SS18V, 5-60 µg). After desalting, peptides were labeled with TMT 10-plex™ reagents according to the manufacturer (Thermo Fisher Scientific, 90110). After quenching of the labeling reaction, the volumes of all samples were adjusted and half the amount of labeled peptides were pooled (for siRNA experiments the whole sample was used), organic solvent removed in a vacuum concentrator at 45°C and reconstituted in 5% acetonitrile containing 20 mM ammonia formate buffer, pH 10 for offline fractionation using high pH reversed phase liquid chromatography (2D-RP/RP-HPLC). Each TMT 10-plex pool contained IP material of 8 different KO cells, one WT sample processed together with the KO cells (WT) and one WT sample (WT pool) that is included in all pools for cross-correlation between individual TMT experiments.

Instead of FASP, the IP samples following siRNA treatment were processed using an adapted Single-pot solid-phase-enhanced sample preparation (SP3) methodology published by Hughes *et. al.*[2]. In short, equal volumes (125 µl/ 6250 µg) of two different kind of paramagnetic

carboxylate modified particles (SpeedBeads 45152105050250 and 65152105050250, GE Healthcare, UK) were mixed, washed three times with 250 µl water and reconstituted to a final concentration of 50 µg/µl with LC-MS grade water (LiChrosolv, MERCK KgaA, Germany). SDS-containing samples from the immunoprecipitation step were reduced with a final concentration of 50 mM DTT and incubated at 60°C for 1 hour. After cooling down to room temperature, reduced cysteins were alkylated with iodoacetamide at a final concentration of 55 mM for 30 min in the dark. For tryptic digestion, 400 µg of mixed beads were added to reduced and alkylated samples, vortexed gently and incubated for 5 min at room temperature. The formed particles-protein complexes were precipitated by addition of acetonitrile to a final concentration of 70% [V/V], mixed briefly before incubating for 18 min at room temperature. Particles were then immobilized using a magnetic rack (DynaMag™-2 Magnet, Thermo Scientific, USA) and supernatant discarded. SDS was removed by washing two times with 200 µl 70% ethanol and one time with 180 µl 100% acetonitrile. After removal of organic solvent, particles were resuspended in 100 µl of 50 mM NH_4HCO_3 and samples digested by incubating with 1 µg of Trypsin overnight at 37°C. Peptides were cleaned up by acidifying the samples to a final concentration of 1% TFA prior to immobilizing the beads on the magnetic rack to perform solid phase extraction of the recovered supernatant using C18 SPE columns (SUM SS18V, NEST group, USA) according to the manufacturer. Peptides were eluted using two times 50 µl 90% acetonitrile, 0.4% formic acid, dried in a vacuum concentrator before reconstitution in 26 µl of 5% formic acid (Suprapur, MERCK KgaA, Germany).

2D-RP/RP Liquid Chromatography Mass Spectrometry

For TMT-labeled samples, two-dimensional liquid chromatography was performed by reverse-phase chromatography at high and low pH. In the first dimension, peptides were separated on a Gemini-NX C18 column (150 × 2 mm, 3 µm, 110 Å, Phenomenex, Torrance, USA) in 20 mM ammonia formate buffer, pH 10, and eluted over 45 min by a 5-70% acetonitrile gradient at 100 µl/min using an Agilent 1200 HPLC system (Agilent Biotechnologies, Palo Alto, CA, USA). Ten time-based fractions were collected, solvent removed in a vacuum concentrator and peptides reconstituted in 5% formic acid for LC-MS/MS analysis. Mass spectrometry was

performed on an Orbitrap Fusion™ Lumos™ Tribrid™ mass spectrometer (Thermo Fisher Scientific, San Jose, CA) coupled to an Agilent 1200 HPLC nanoflow system (Agilent Biotechnologies, Palo Alto, CA) via Nanospray Flex™ Ion source interface. Tryptic peptides were loaded onto a trap column (Zorbax 300SB-C18 5 µm, 5 × 0.3 mm, Agilent Biotechnologies) at a flow rate of 45 µl/min using 0.1% TFA as loading buffer. After loading, the trap column was switched in-line with a 25 cm, 75 µm inner diameter analytical column (packed in-house with ReproSil-Pur 120 C18-AQ, 3 µm, Dr. Maisch, Ammerbuch-Entringen, Germany). Mobile-phase A consisted of 0.4% formic acid in water and mobile-phase B of 0.4% formic acid in a mix of 90% acetonitrile and 10% water. The flow rate was set to 250 nl/min and a 120 min gradient was used (6 to 30% solvent B within 100 min, 30 to 65% solvent B within 20 min and, 65 to 100% solvent B within 1 min, 100% solvent B for 8 min before re-equilibrating at 6% solvent B for 16 min). Analysis was performed in a data-dependent acquisition mode using the multi-notch MS^3-based TMT method (SPS-MS^3) described by McAlister *et al.*[3]. MS^1 spectra were acquired within a mass range of 375 - 1650 m/z in the orbitrap at a resolution of 120000 (at 200 Th). Automatic gain control (AGC) was set to a target of 2×10^5 and a maximum injection time of 50 ms. Precursor ions for MS^2/MS^3 analysis were selected using a max. 3 s cycle time scan approach. MS^2 spectra were acquired in the linear quadrupole ion trap (IT) using a quadrupole isolation window of 0.7 Da; collision induced dissociation (CID) for fragmentation; a normalized collision energy (NCE) of 35%; an AGC target of 1×10^4; and a maximum injection time of 50 ms. For TMT quantitation, each MS^2 scan followed a SPS-MS^3 scan of the same precursor ion using the multiple frequency notches approach[3]. For MS^3 scans, the quadrupole isolation window was set to 2 Da and the top five most intense MS^2 fragment ions were isolated by SPS for fragmentation using higher energy collision-induced dissociation (HCD) with an NCE of 65%. AGC was set to a target of 1×10^5 and a maximum injection time of 150 ms. Resulting fragment ions were analyzed in the orbitrap at a resolution of 50000 (at 200 Th). Dynamic exclusion for selected ions was 20 s. A single lock mass at *m/z* 445.120024 was employed[4]. Xcalibur version 4.0.0 and Tune 2.1.1565.24 were used to operate the instrument.

Unlabeled IP samples were analyzed in a 1D 'shotgun' LC-MS/MS fashion on the following instruments: Hybrid linear trap quadrupole (LTQ) Orbitrap Velos, Q Exactive™ or Orbitrap Fusion™ Lumos™ Tribrid™ mass spectrometer (Thermo Fisher Scientific, San Jose, CA) coupled to either an Agilent 1200 (Agilent Biotechnologies, Palo Alto, CA) or Dionex U3000RSLC U/HPLC nanoflow system (Thermo Fisher Scientific, San Jose, CA) via Nanospray Flex™ Ion source interface. Instrument settings are shown in the table below:

	LTQ-Orbitrap Velos Agilent 1200 nano	Q Exactive Agilent 1200 nano	Fusion Lumos U3000 RSLCnano
Trap column/ loading	Zorbax 300SB-C18 5 µm, 5 × 0.3 mm, 45 µl/min with 0.1% TFA	Acclaim™ PepMap™ 100 C18, 3µm, 5 × 0.3 mm; 10 µl/min with 0.1% TFA	Acclaim™ PepMap™ 100 C18, 3µm, 5 × 0.3 mm; 10 µl/min with 0.1% TFA
Analytical column	25 cm, 75 µm I.D. packed in-house with ReproSil-Pur 120 C18-AQ, 3 µm, Dr. Maisch	25 cm, 75 µm I.D. packed in-house with ReproSil-Pur 120 C18-AQ, 3 µm, Dr. Maisch	25 cm, 75 µm I.D. packed in-house with ReproSil-Pur 120 C18-AQ, 3 µm, Dr. Maisch
Buffer A/B	A: 0.4% FA B: 90% ACN, 0.4% FA	A: 0.4% FA B: 90% ACN, 0.4% FA	A: 0.4% FA B: 90% ACN, 0.4% FA
Gradient time	60 min	90 min	90 min
Flow rate	250 nl/min	230 nl/min	230 nl/min
MS^1 scan	• Orbitrap detector • 60000 resolution (at m/z 400) • 350-1800 m/z scan range • Target of 1×10^6 • max injection time of 500 ms	• Orbitrap detector • 70000 resolution (at m/z 200) • 375-1650 m/z scan range • Target of 1×10^6 • max injection time of 50 ms	• Orbitrap detector • 120000 resolution (at m/z 200) • 375-1650 m/z scan range • Target of 2×10^5 • max injection time of 50 ms
MS^2 scans	• Linear ion trap (IT) detector • Top15 • Threshold of 2000 cts • AGC target of 1×10^4 • max injection time of 50 ms • isolation width of 2.0 m/z • CID with NCE of 30%	• Orbitrap (FT) detector • 17,500 resolution (at m/z 200) • Top10 • Threshold of 1800 cts • AGC target of 1×10^5 • max injection time of 110 ms • isolation width of 2.0 m/z • HCD with NCE of 28%	• Linear ion trap (IT) • Rapid scan rate • Top10 • Threshold of 1800 cts • AGC target of 1×10^4 • max injection time of 50 ms • isolation width of 1.6 m/z • HCD with NCE of 30%
Dynamic exclusion	60 sec with ±10 ppm	20 sec with ±10 ppm	60 sec with ±10 ppm
Lock mass	Enabled at m/z of 445.120024	Enabled at m/z of 445.120024	Enabled at m/z of 445.120024
IP	SMARCA4, ARID1A	ARID2	SMARCC1, SMARCC2, SMARCE1, SMARCB1, BRD9

MS data analyses

Acquired raw data files were processed using the Proteome Discoverer 2.2.0.388 platform, utilizing the database search engine Sequest HT. Percolator V3.0 was used to remove false positives with a false discovery rate (FDR) of 1% on peptide and protein level under strict conditions. Searches were performed with full tryptic digestion against the human SwissProt database v2017.07 (20158 sequences appended with known contaminants and rabbit IgG protein sequence) with up to two miscleavage sites. Oxidation (+15.9949 Da) of methionine, phosphorylation (+79.966 Da) of serine, threonine, and tyrosine, and acetylation (+42.011 Da) of protein N-termini were set as variable modifications, whilst carbamidomethylation (+57.0214 Da) of cysteine residues were set as fixed modification. Additionally, for TMT multiplexed samples, TMT 6-plex label of peptide N-termini and lysine residues were set as fixed modification. Data was searched with mass tolerances of ±10 ppm and 0.6 Da on the precursor and fragment ions (CID), respectively. Results were filtered to include peptide spectrum matches (PSMs) with Sequest HT cross-correlation factor (Xcorr) scores of ≥ 1 and high protein confidence (1% FDR in Percolator). PSMs with precursor isolation interference values of ≥ 50% and average TMT-reporter ion signal-to-noise values (S/N) ≤ 10 were excluded from quantitation, moreover peptides containing a phosphorylated and acetylated residue were not used for quantitation of proteins. Isotopic impurity correction was applied and the TMT channels were normalized to yield equal bait abundance. The total abundance of each protein summed across all TMT channels were estimated using intensity-based absolute quantification, iBAQ algorithm[5] (the MS1 intensities of the unique and razor precursor peptides that mapped to each protein were summed and divided by the number of theoretically observable peptides). The numbers of theoretically observable peptides were calculated by isobar package[6]. For comparison of protein abundancies across immunoprecipitated samples with various baits, the Top3 methodology published by Silva et al. was applied[7].

For statistical analysis, the empirical distribution of observed log ratios between two WT replicates (WT.R) was fitted by a normal distribution. The ratio *WT.R1/WT.R2* can be calculated by utilizing the common *WT* channel (WT pool) present in each TMT experiment as

$\frac{WT.R1}{WT.R2} = \frac{WT.R1/WT\ pool}{WT.R2/WT\ pool}$. P-values of observed TMT-ratios were calculated from the corresponding distribution function of the fitted normal distribution. P-values from the two TMT experiments were then combined using Fisher's method and corrected for FDR by Benjamini-Hochberg procedure. Resulting FDR values smaller than 1%, 0.1%, or 0.01% are shown by corresponding number of asterisks in the heatmaps.

To identify potential new interactors of BAF complexes, the following interaction score for a protein *P* was used:

$$score(P) = \min\left(0.1 + 3\big(1 - cor(rA, rB)\big),\ \max\left(0.1, \sqrt{\frac{\sum_{i=1}^{N}(rA_i - rB_i)^2}{N}}\right)\right), \qquad (1)$$

where *rA* and *rB* are vectors of observed ratios of the protein *P* across *N* knock-out conditions against the corresponding WT.R abundance of the protein *P* in replicate *A* or *B*, respectively. The lower the score, the more likely the protein *P* is an interactor of BAF complexes. By the definition (1), the minimum possible interaction score is 0.1.

Subunit interaction analysis from IP-MS data

We implemented a genetic algorithm to identify the most likely pairwise interactions and competitions among the subunits of the BAF and PBAF complexes, using the IP-MS data as input. First, we apply it only for the ARID1A IP and the 25 enriched subunits (i.e. ACTL6B, ARID2, BRD7 and PBRM1 are ignored). Then we apply the algorithm on all 29 BAF and PBAF subunits for the SMARCA4 IP and for both ARID1A and SMARCA4 IP data.

The algorithm is based on the following simplified model: Each subunit can interact or compete with one or several other subunits. The full complex configuration can then be represented as a structure graph with subunits as nodes and two edge types, indicating an interaction or competition between two subunits.

Considering only the interaction links, the knock-out of a particular subunit can then be understood as a removal of the respective node from the graph. Depending on the overall structure of the graph and the particular connections of the node, its removal may also leave

several other nodes disconnected from the rest of the graph. Within this model, we expect that subunits that are no longer connected to the graph component that contains ARID1A or SMARCA4 due to the knock-out of another subunit should be depleted in the respective pulldown experiment. Likewise, we expect that subunits that compete with the knocked-out subunit should be enriched (as well as all subunits connected to it). This allows us to compute the expected outcome of each knock-out for a particular graph structure, which can then be compared to the actual outcome as measured in the IP-MS experiments.

We use a threshold in FDR and binarize the measured data as increased (FC > 1) or decreased subunit abundance (FC < 1), allowing us to use the Jaccard similarity coefficient between experimental and predicted changes according to the model for a given structure graph. The Jaccard coefficient is defined as the number of abundance changes that are shared between prediction and measurement divided by their union and can be used as a measure of “fitness” of a given candidate structure graph in our genetic algorithm.

The algorithm (implemented in the Julia programming language, version 0.6.2), operates on a population of candidate structure graphs in which all subunits should be (directly or indirectly) connected. Four mutation types are used in our simulations: insertion or deletion of an interaction, swap of interaction partners and change in competition. We disregard mutations that do not maintain the overall connectivity of the structure graph or that create an interaction between competing subunits.

We can test the performance of our algorithm by applying it to randomly generated structures with known outcomes for both pulldowns. Our simulations with runs of 10000 generations for populations of 500 graphs that were fitted on the abundance changes expected for 200 generated structures show that our implementation indeed scans the space of solutions of interest very efficiently. We observe near perfect final fitness of the best structure in the population (0.99 on average). Note however, that in most cases the number of inferred interactions is lower than in the actual model structure (on average 61 and 197 interactions, respectively). This means that in highly connected complexes a subset of all interactions can already explain the observed abundance changes. We further find that structures with less

interactions are more difficult to infer: the simulations with a fitness lower than 0.95 correspond to structures with on average 57 interactions, whereas the overall average among the 200 generated structures is 197 interactions. There is also a difference in how well competitions and interactions are predicted (95% and 49% of true positives, respectively). Taken together, we conclude that aggregating the results of several independent runs on the experimental results can circumvent the high false positive rate in inferred interactions.

We used three different initial configurations in our simulations: (i) completely random interactions and competitions, (ii) competitions based on sequence similarity, and (iii) interactions and competitions based on prior knowledge.

Sequences for the 29 subunits were obtained on 2018-03-23 by querying BioMart[8] by HGNC gene symbols for human peptides sequences and taking the longest sequence available for each protein. Global pairwise alignments were conducted between these sequences using the BioAlignments 0.2.0 package, with a cost model using BLOSUM80 for substitutions and -5 and -1 penalties for gap opening and extension, respectively. The best scoring alignments for each combination were then filtered to keep alignments with more than 40% of the aligned amino acids pairs matched. This led to the following potential competition classes, based on sequence similarity: SMARCA4-SMARCA2, ARID1A-ARID1B, SMARCD1-SMARCD2-SMARCD3, DPF1-DPF2-DPF3, SMARCC1-SMARCC2, SS18-SS18L1, ACTL6A-ACTL6B and BCL11A-BCL11B. All these groups correspond to paralogous genes.

The prior knowledge used in the initial configurations included relations established in the literature or suggested from our experiments. This includes all of the competitions inferred by sequence similarity as well as PHF10-DPF1-DPF2-DPF3 and BCL7A-BCL7B-BCL7C, and interactions between SMARCC1-SMARCB1[9], SMARCE1-SMARCC1[10], SMARCE1-SMARCC2[11], SMARCA4-ACTB, SMARCA4-ACTL6A, SMARCA4-ACTL6B, SMARCA2-ACTB, SMARCA2-ACTL6A and SMARCA2-ACTL6B[11-13].

To avoid overfitting of the simulated graphs to potential false negatives or false positives due to a particular FDR cut-off choice on abundance changes in the IP-MS data, four different cut-offs were used: 0.01, 0.05, 0.001 and 0.005.

For the simulations based on ARID1A IP only, SMARCA4 only and those on combined ARID1A and SMARCA4 IPs, for each of the 12 possible combinations between initial condition and FDR cut-off, 25 independent runs were conducted, for populations of 500 graphs, with 10000 generations and a mutation rate of 0.026 for each of the mutation type (competition change, edge addition, deletion and swap), yielding a final population of 150000 graphs, with fitness in range [0.18, 0.66] for ARID1A IP only, [0.20, 0.58] for SMARCA4 IP only and [0.19, 0.53] for combined IP data. These graphs were then integrated in a weighted frequency matrix for each possible competition and interaction, by summing the fitnesses of all the graphs having this relation and normalizing each weight, so that a weight of 1 corresponds to a relation observed in all of the simulated graphs.

To assess the relevance of the frequently observed edges, we performed simulations with randomly reshuffled abundance changes for both IP-MS experiments, keeping only the decrease in abundance observed in a subunit for its own knock-out fixed. Rerunning the algorithm 15 times for each of the 12 initial conditions, we find that the distribution of the rates at which each interaction or competition is found is more concentrated around smaller values than what is observed when running the algorithm on the actual data. Competitions and interactions are never found in more than 11% and 19%, respectively, of the structures generated on the shuffled data. We conclude that the interactions and competitions that were found at a much higher rate when running the algorithm on the real experimental results cannot be attributed to chance alone. The fitnesses are also lower for simulations on the shuffled data, with a median fitness after 10000 generations of 0.30 on average, compared to 0.40 for the original data, suggesting that the model describes better the latter.

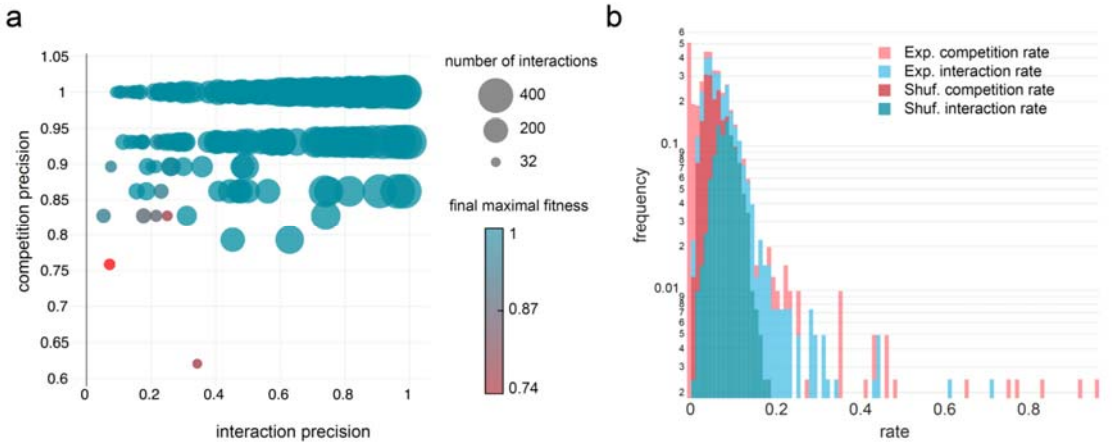

Supplementary Note Fig. 1 | Evaluation of the performance of the genetic algorithm using randomly generated structures with known interactions and competitions.
(a) Precision (i.e. the proportion of true positives among all positives) of interactions and competitions of the best solution inferred from abundance changes that correspond to 200 randomly generated structures. Each point corresponds to one random structure, point size is proportional to its number of interactions, and color indicates the fitness of the best solution identified through our algorithm. The performance is generally better for denser structure and for competition than for interactions. (b) Comparison of the rates at which individual competitions and interactions occur among different realizations of the algorithm for the original experimental results (*Exp.*) and for randomly shuffled data (*Shuf.*). In the shuffled data, the rates are generally confined to relatively low values of less than ~0.2, indicating that the high rates achieved on the original data correspond to true interactions/ competitions.

We assessed the coherence between the structural estimation from SMARCA4 and ARID1A IPs and the results from another experiment, where we performed IP-MS after siRNA knock-down of a BAF subunit on top of the knock-out of another BAF subunit. First, we extracted the weighted adjacency matrix from the structural interaction network previously generated, coined A_{WT}. To quantify the connectivity of a subunit to the pulled sub-complex according to the network model, we performed a random walk on this network starting from the SMARCC1 node. We obtained a transition matrix M_{WT} by normalizing A_{WT} by column. The expectation of arrival node after 1000 steps L_{WT} was then computed as $L_{WT}=(M_{WT})^{1000}I$ with I the indicator vector of SMARCC1. We then modeled each perturbation (KO combined with siRNA) by disconnecting the nodes corresponding to the targets of the KO and of the siRNA from the interaction network, leading to a vector L, which characterizes the connectivity of the nodes to the network component including the SMARCC1 node. The ratio $\frac{L}{L_{WT}}$ was used as an estimator of the abundance changes occurring to each subunit for this genetic perturbation.

On the other hand, the measured protein abundances were normalized on SMARCC1 and scaled per protein. The ratio over WT was computed for each perturbation. A paired t-test was performed to quantify significance of abundance changes between WT cells and each perturbation, where measurements were paired by TMT experiment of origin. The condition-wide FDR was inferred for all proteins.

The correlation between experimental and modeled abundance changes was then assessed using several metrics: (i) Pearson correlation, (ii) Spearman correlation, (iii) Kendall correlation and (iv) Cohen's kappa for predicted ratios inferior or superior to 1.

	SMARCA4 KO siNTC	SMARCA4 KO siSMARCA2	SMARCA4 KO siARID2	SMARCA4 KO siACTB	ARID2 KO siNTC	ARID2 KO siSMARCA4	ACTB KO siNTC	ACTB KO siSMARCA4
n=	19	14	21	14	14	24	15	19
Pearson correlation	0.309554413	0.255884932	0.309647713	0.271706108	0.570646111	0.338316532	0.356927651	0.327724213
Spearman correlation	0.231578947	0.195604396	0.468983461	0.564835165	0.371428571	0.467492944	0.625	0.564912281
Kendall correlation	0.157894737	0.120879121	0.300716847	0.428571429	0.230769231	0.337568614	0.447619048	0.426900585
Cohen's kappa	0.222222222	0.071428571	0.210526316	0.099009901	0.805970149	0.326359833	0.081967213	0.111111111

The correlation values were computed by perturbation, while ignoring subunits with an FDR > 0.61, in order to remove the most insignificant changes while retaining subunits in all conditions. Increasing the predicted values for subunits losing a competing subunit or assessing network connectivity more specifically to SMARCC1 using a random walk with restart did not improve the correlation with the observed abundances.

References

1. Wisniewski, J.R., Zougman, A., Nagaraj, N. & Mann, M. Universal sample preparation method for proteome analysis. *Nat Methods* **6**, 359-62 (2009).
2. Hughes, C.S. *et al.* Ultrasensitive proteome analysis using paramagnetic bead technology. *Mol Syst Biol* **10**, 757 (2014).
3. McAlister, G.C. *et al.* MultiNotch MS3 enables accurate, sensitive, and multiplexed detection of differential expression across cancer cell line proteomes. *Anal Chem* **86**, 7150-8 (2014).
4. Olsen, J.V. *et al.* Parts per million mass accuracy on an Orbitrap mass spectrometer via lock mass injection into a C-trap. *Mol Cell Proteomics* **4**, 2010-21 (2005).
5. Schwanhausser, B. *et al.* Global quantification of mammalian gene expression control. *Nature* **473**, 337-42 (2011).
6. Breitwieser, F.P. *et al.* General statistical modeling of data from protein relative expression isobaric tags. *J Proteome Res* **10**, 2758-66 (2011).
7. Silva, J.C., Gorenstein, M.V., Li, G.Z., Vissers, J.P. & Geromanos, S.J. Absolute quantification of proteins by LCMSE: a virtue of parallel MS acquisition. *Mol Cell Proteomics* **5**, 144-56 (2006).
8. Zerbino, D.R. *et al.* Ensembl 2018. *Nucleic Acids Res* **46**, D754-D761 (2018).

9. Yan, L., Xie, S., Du, Y. & Qian, C. Structural Insights into BAF47 and BAF155 Complex Formation. *J Mol Biol* **429**, 1650-1660 (2017).
10. Chen, J. & Archer, T.K. Regulating SWI/SNF subunit levels via protein-protein interactions and proteasomal degradation: BAF155 and BAF170 limit expression of BAF57. *Mol Cell Biol* **25**, 9016-27 (2005).
11. Tang, L., Nogales, E. & Ciferri, C. Structure and function of SWI/SNF chromatin remodeling complexes and mechanistic implications for transcription. *Prog Biophys Mol Biol* **102**, 122-8 (2010).
12. Zhao, K. *et al.* Rapid and phosphoinositol-dependent binding of the SWI/SNF-like BAF complex to chromatin after T lymphocyte receptor signaling. *Cell* **95**, 625-36 (1998).
13. Szerlong, H. *et al.* The HSA domain binds nuclear actin-related proteins to regulate chromatin-remodeling ATPases. *Nat Struct Mol Biol* **15**, 469-76 (2008).

2. Additional Results

2.1 CRISPR/Cas9 editing efficiency in cancer cell lines used for the multicolor competition assay

In order to test the CRISPR/Cas9 editing efficiency in the cell lines used for the multicolor competition assay (MCA), we selected three cell lines with low or no synthetic lethal effect and three with a strong effect in the experiments performed in this study. We transduced them with each gRNA separately and selected the transduced cells with puromycin before assessing the expression of the targeted BAF subunit by Western blot.

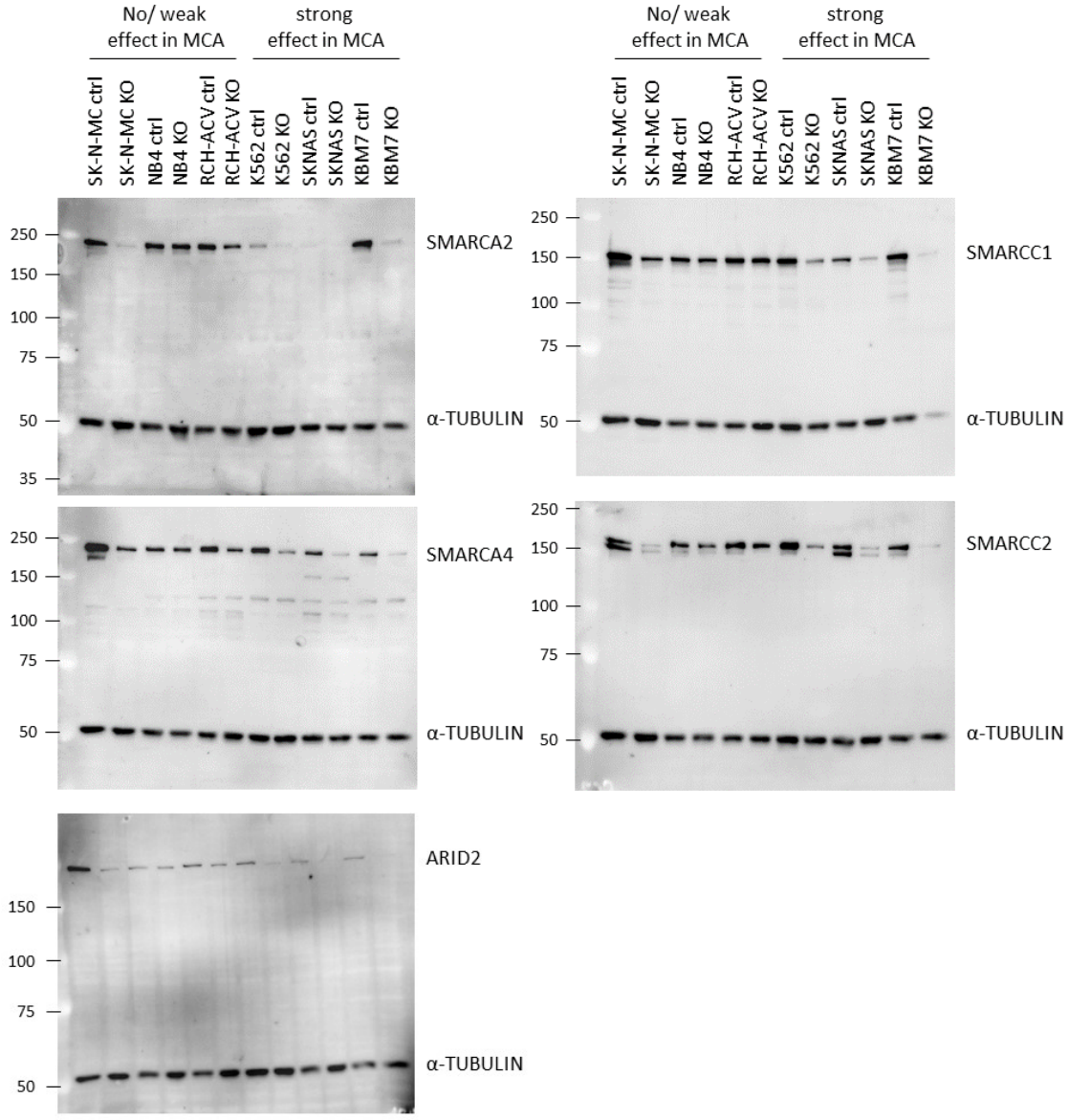

Supplementary Note Fig. 2 | Western blot analyses to check CRISPR/Cas9 editing efficiency.
Indicated cell lines were transduced either with a control vector (expressing fluorescent marker, but no gRNA; ctrl) or a gRNA targeting the BAF subunit for which the blot is stained (KO). α-TUBULIN was used as a loading control.

3. Full Western Blots

3.1 Figure 1b

Loading scheme for all plots:

	Loading 1														
Lane	1	2	3	4	5	6	7	8	9	10	11	12	13	14	15
Sample	Marker	WT	ARID1A 618-10	ARID1A 618-3	ARID1B 582-7	ARID2 907-9	SMARCA 2 4055-12	SMARCA 4 2878-4	SMARCA 4 2878-6	SMARCD 1 2478-6	SMARCD 2 2782-10	SMARCD 3 2480-12	SMARCC1 2476-12	SMARCC2 6062-10	SMARCC2 2783-11

	Loading 2														
Lane	1	2	3	4	5	6	7	8	9	10	11	12	13	14	15
Sample	M	WT	ACTB 2471-10	BCL7A 2434-10	BCL7B 4278-8	BCL11A 2426-10	BCL11B 2432-10	DPF1 2779-11	DPF2 2777-4	DPF3 2776-1	PHF10 2778-11	PBRM1 1135-10	BRD7 923-10	BRD9 934-10	ARID2 907-9

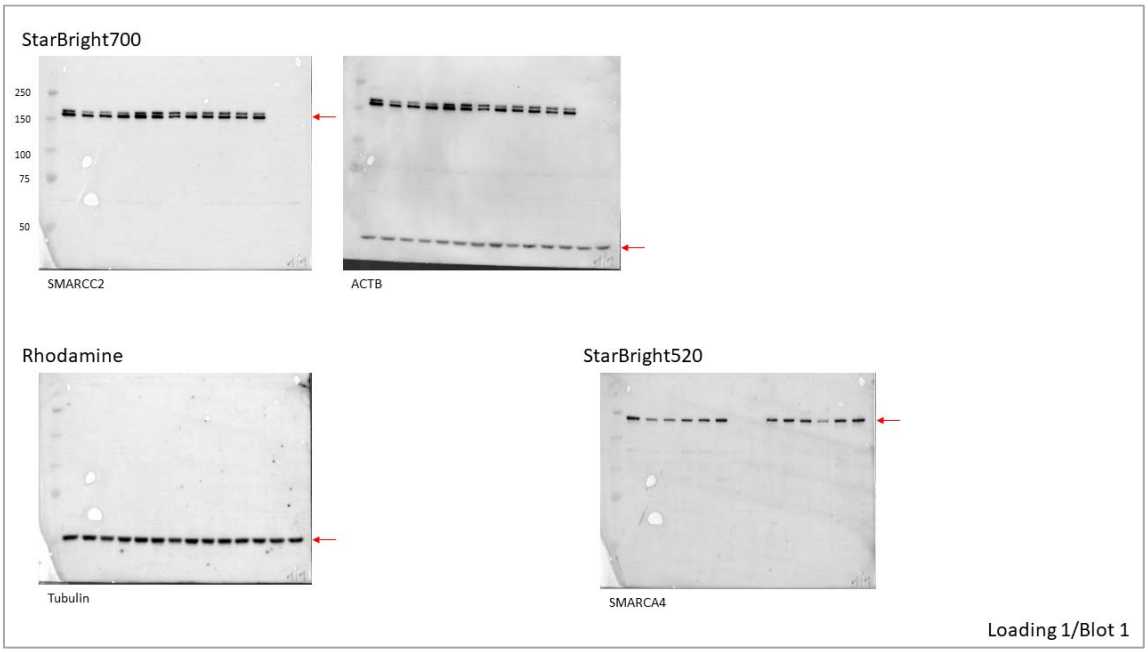

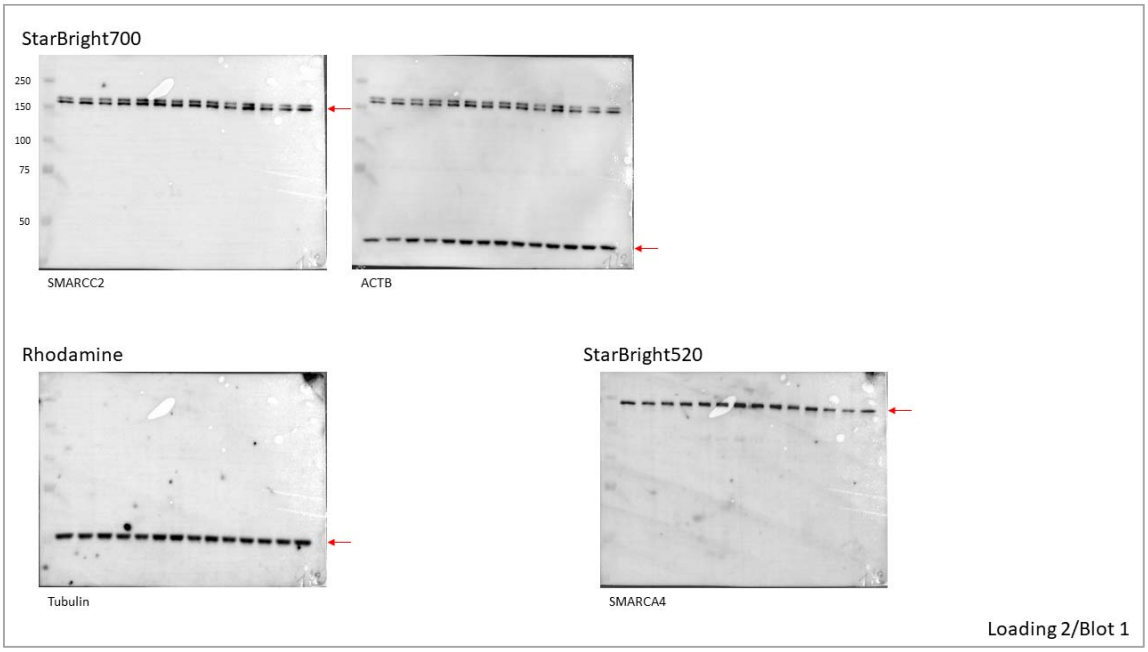

StarBright700

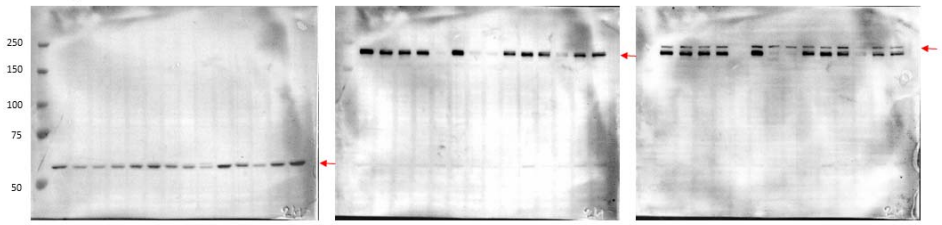

SMARCD2, santa cruz PBRM1 ARID2

Rhodamine

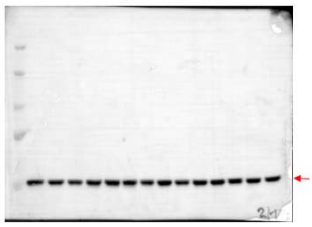

Tubulin

Loading 1/Blot 2

StarBright700

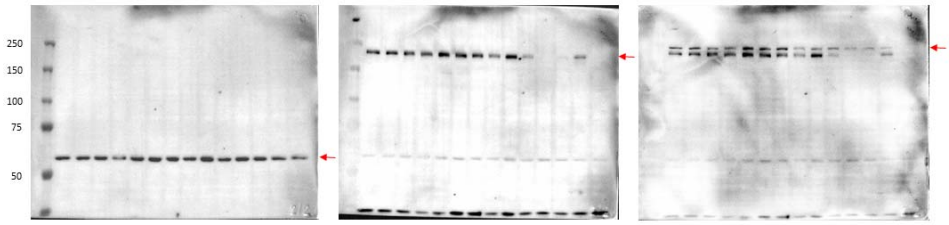

SMARCD2, santa cruz PBRM1 ARID2

Rhodamine

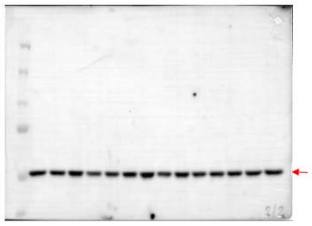

Tubulin

Loading 2/Blot 2

StarBright700

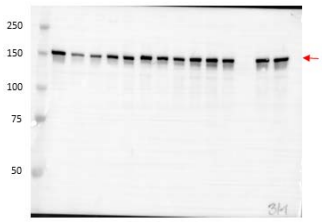

SMARCC1

Rhodamine

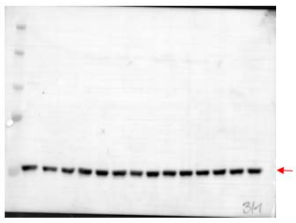

Tubulin

Loading 1/Blot 3

StarBright700

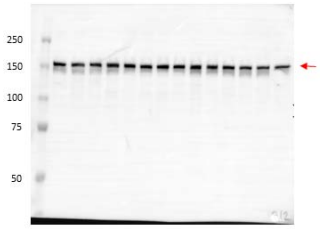

SMARCC1

Rhodamine

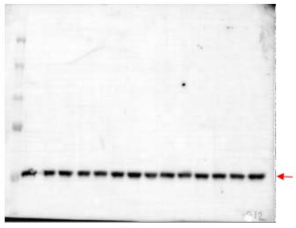

Tubulin

Loading 2/Blot 3

StarBright700

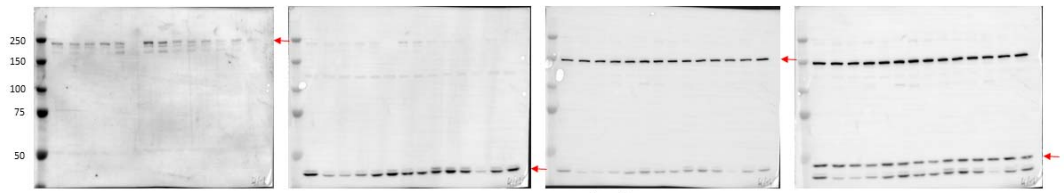

SMARCA2 SMARCB1 BRD4 (2 sec) ACTL6A

Rhodamine

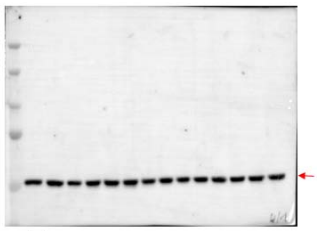

Tubulin

StarBright520

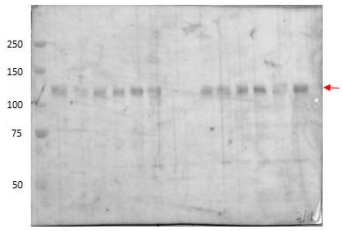

BCL11A

Loading 1/Blot 4

StarBright700

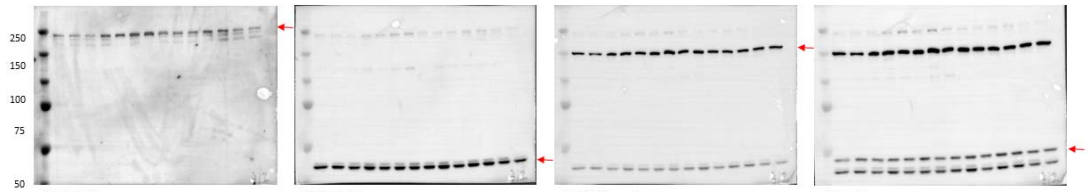

SMARCA2 SMARCB1 BRD4 (2 sec) ACTL6A

Rhodamine

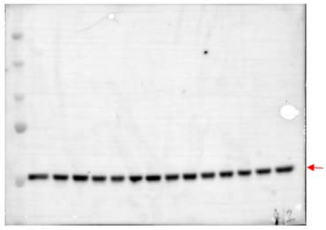

Tubulin

StarBright520

BCL11A

Loading 2/Blot 4

StarBright700

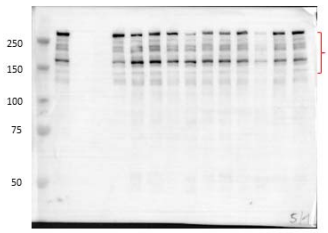

ARID1A

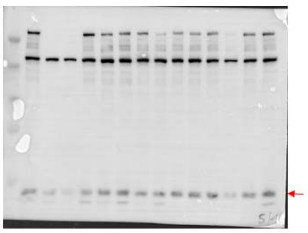

DPF2

StarBright520

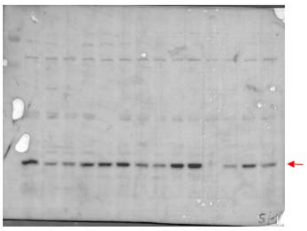

SMARCD3

Rhodamine

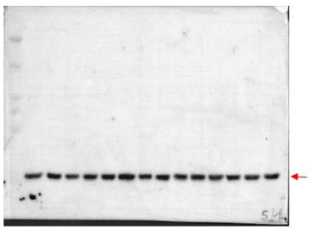

Tubulin

Loading 1/Blot 5

StarBright700

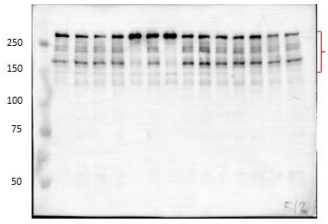

ARID1A

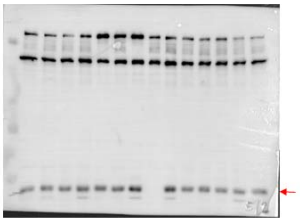

DPF2

StarBright520

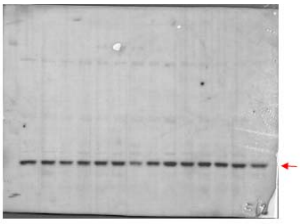

SMARCD3

Rhodamine

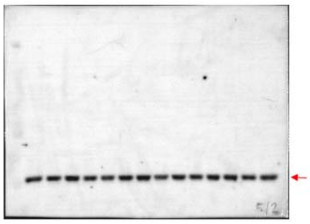

Tubulin

Loading 2/Blot 5

StarBright520

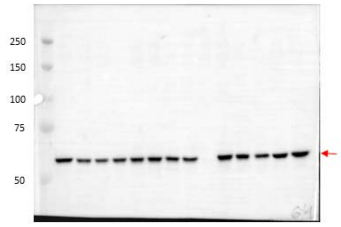

SMARCD1

StarBright700

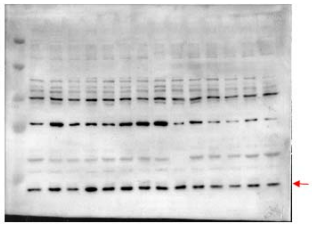

SS18

Rhodamine

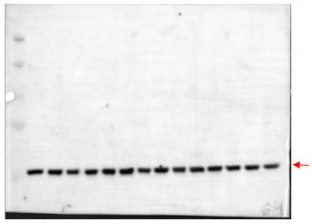

Tubulin

Loading 1/Blot 6

StarBright520

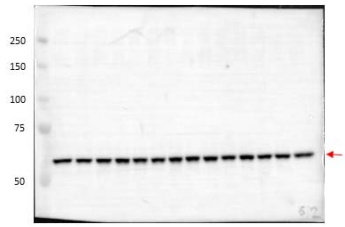

SMARCD1

StarBright700

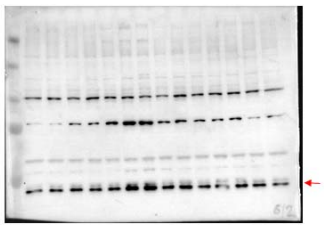

SS18

Rhodamine

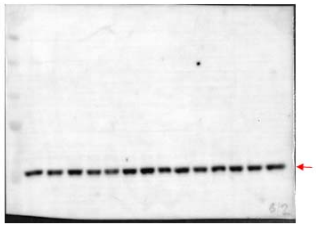

Tubulin

Loading 2/Blot 6

StarBright700

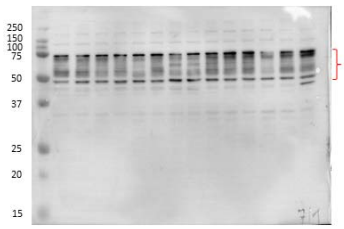

PHF10

Rhodamine

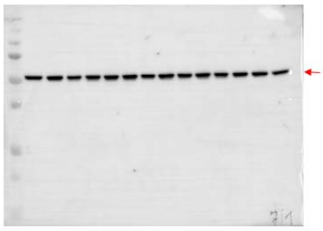

Tubulin

Loading 1/Blot 7

StarBright700

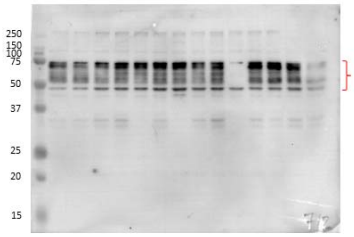

PHF10

Rhodamine

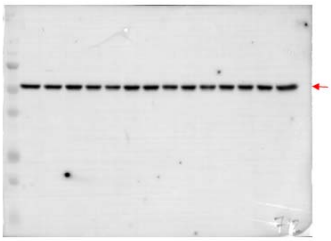

Tubulin

Loading 2/Blot 7

StarBright700

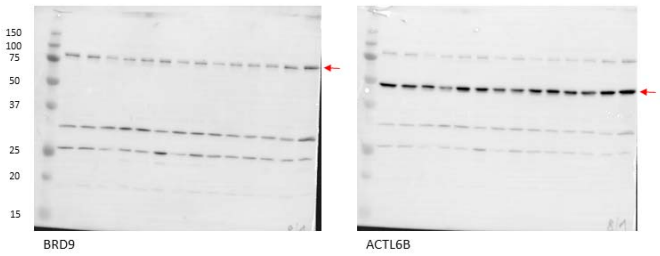

Rhodamine

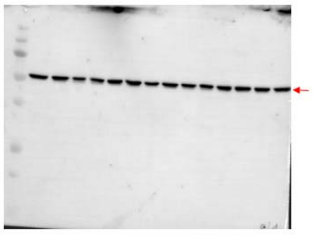

Loading 1/Blot 8

StarBright700

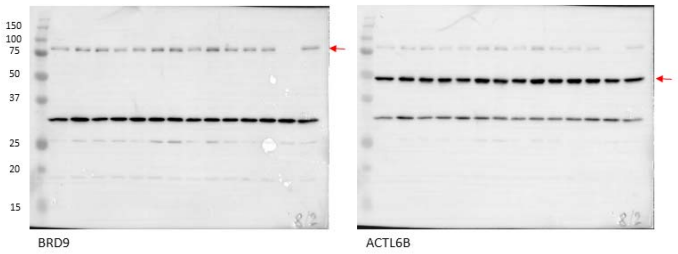

Rhodamine

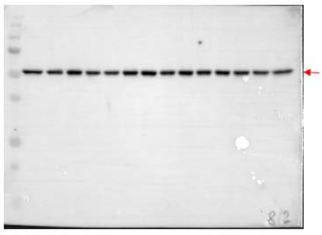

Loading 2/Blot 8

StarBright700

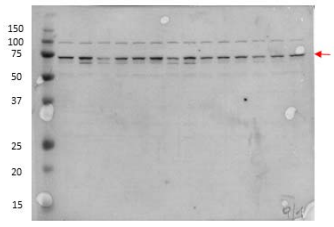

SMARCD2, abcam

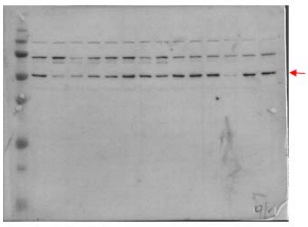

SMARCE1

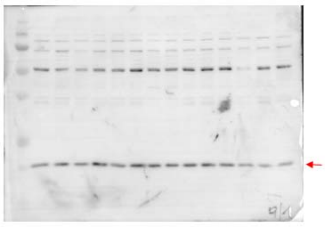

BCL7C

Rhodamine

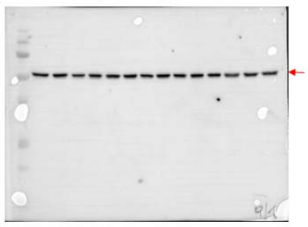

Tubulin

Loading 1/Blot 9

StarBright700

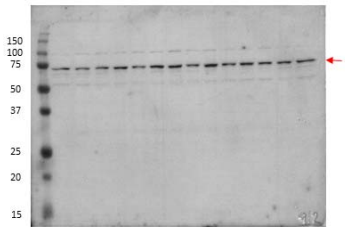

SMARCD2, abcam

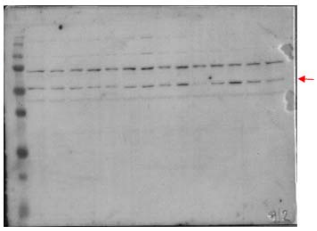

SMARCE1

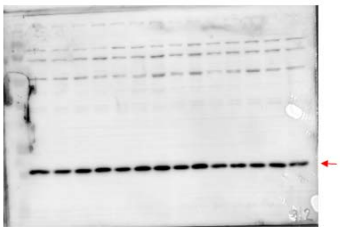

BCL7C

Rhodamine

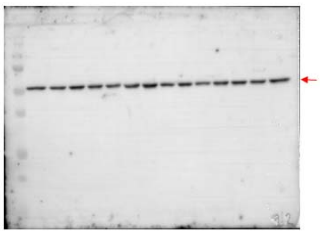

Tubulin

Loading 2/Blot 9

StarBright700

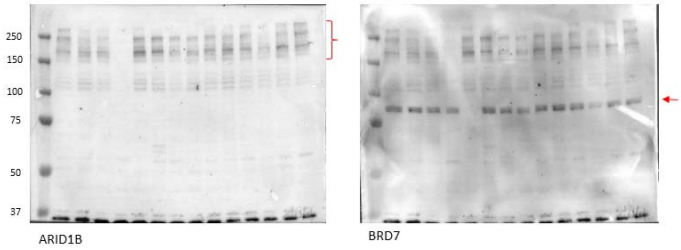

Rhodamine

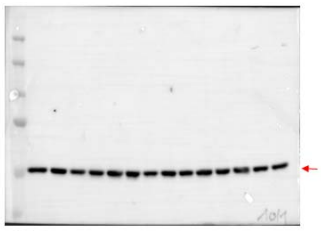

Loading 1/Blot 10

StarBright700

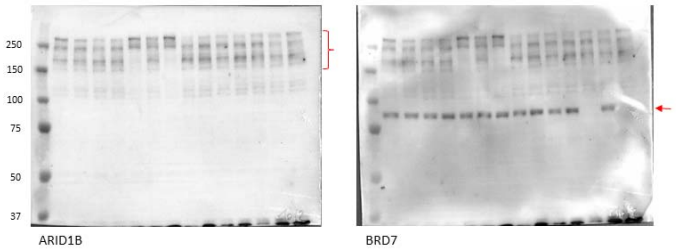

Rhodamine

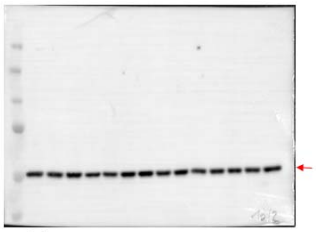

Loading 2/Blot 10

3.2 Supplementary figure 11f

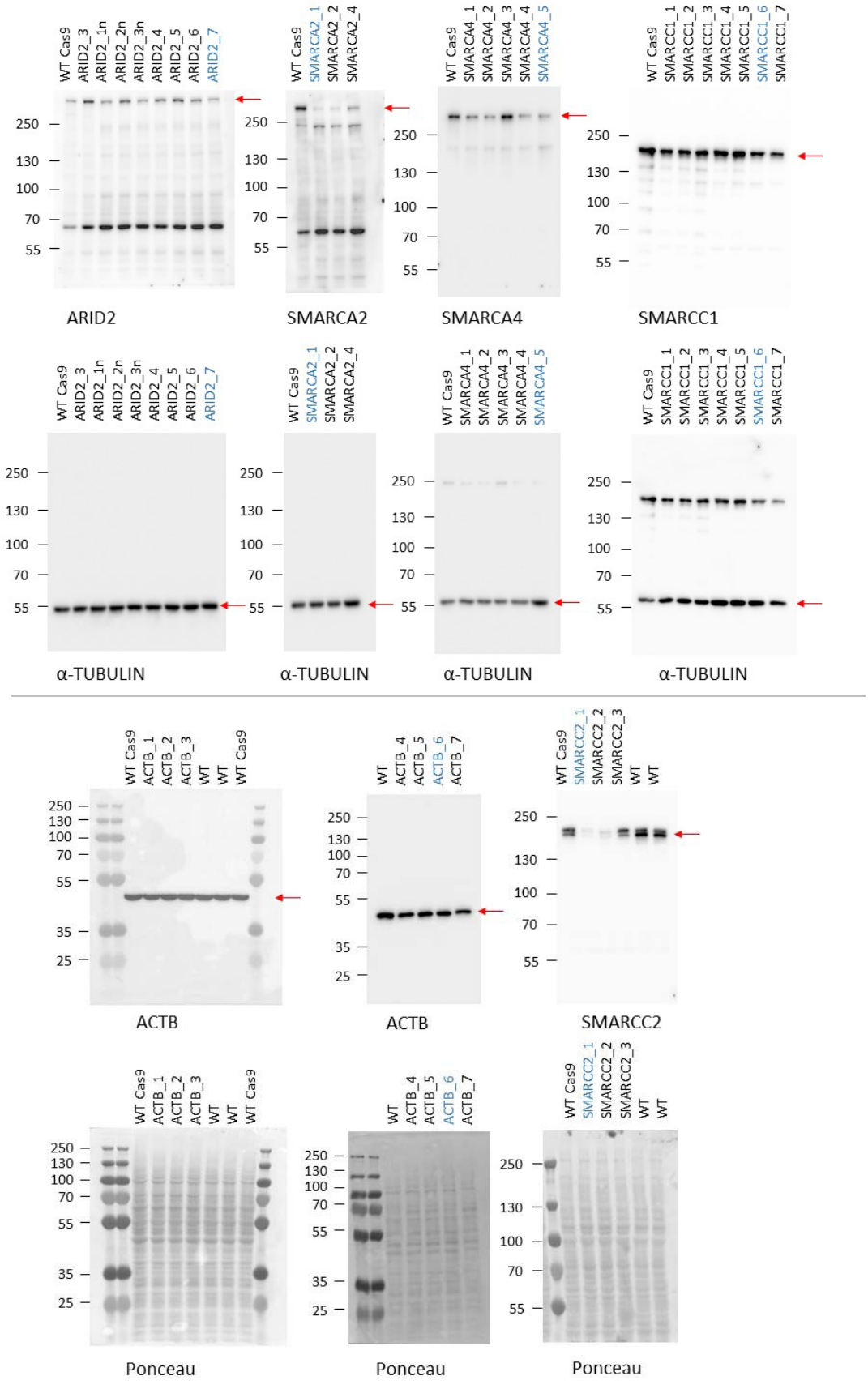

3.3 Supplementary figure 12a

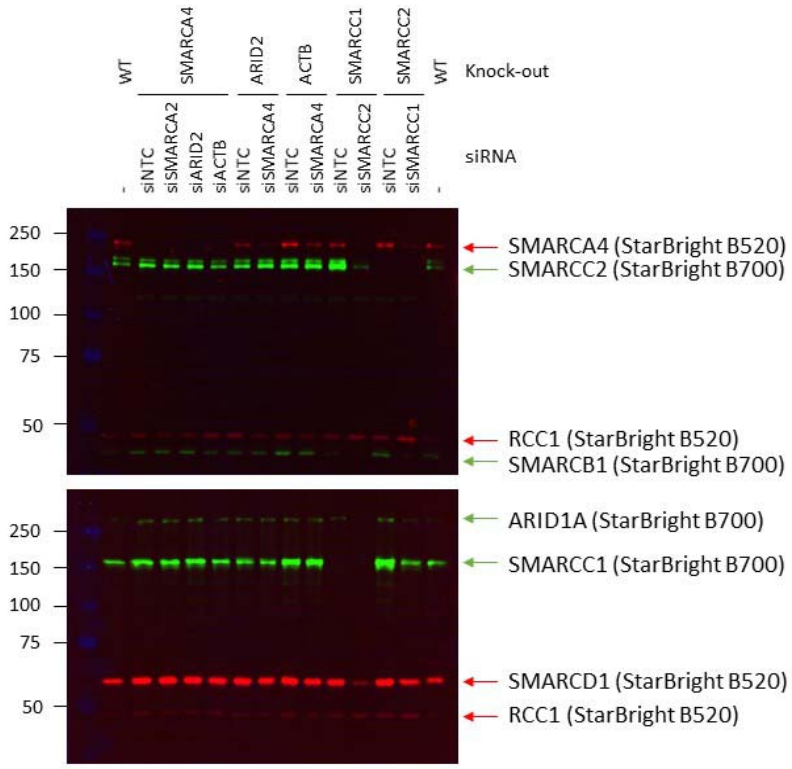

3.4 Supplementary figure 15a

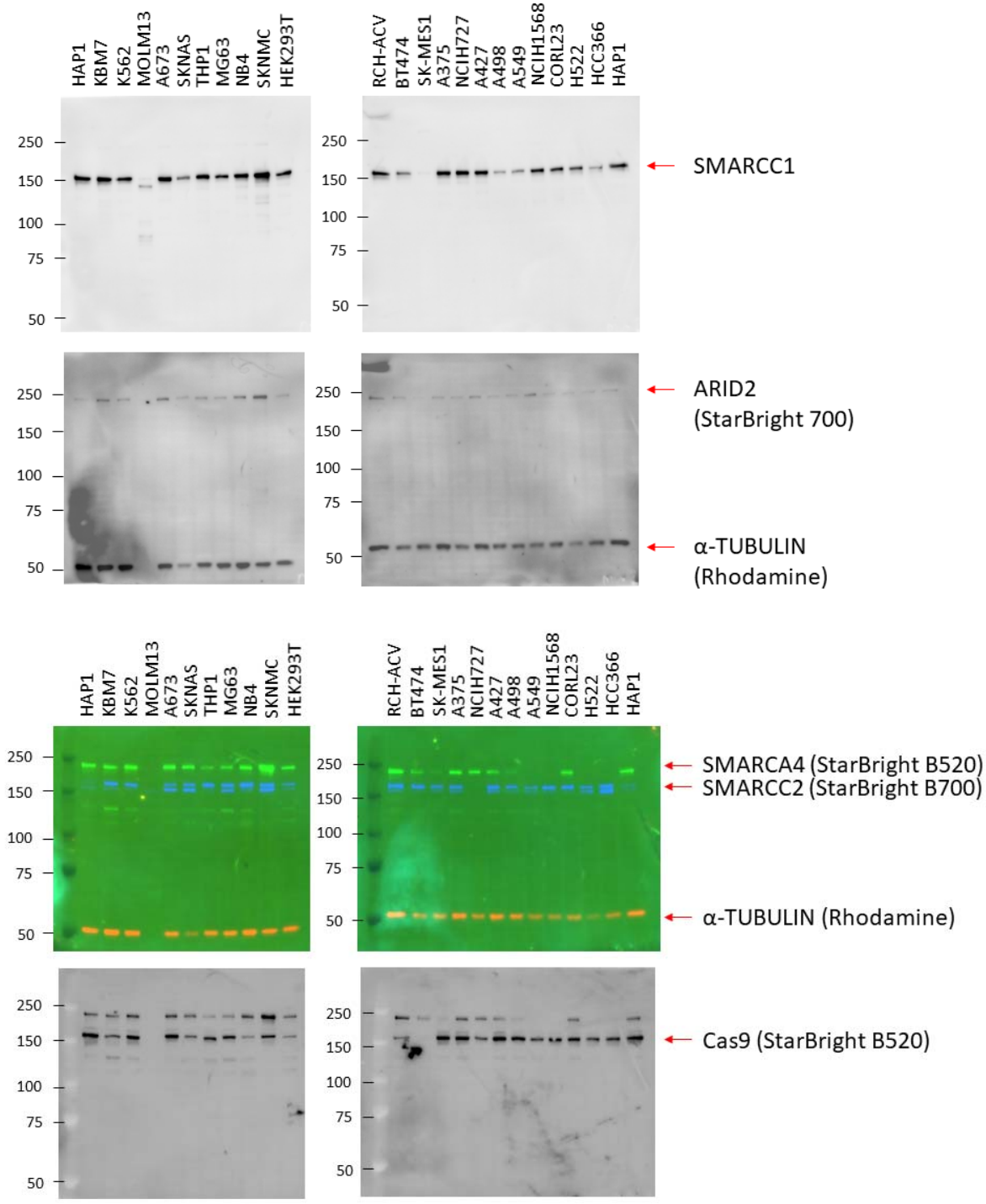

4. Alternative names for BAF subunits

Gene	alternative names
SMARCA2	(H)BRM, SNF2L2, BAF190B, SNF2, SWI2
SMARCA4	BAF190A, BRG1, SNF2LB,SWI2, SNF2
BRD7	CELTIX1, NAG4
BRD9	
PBRM1	BAF180, PB1
ARID1A	BAF250(A), SMARCF1, C1orf4
ARID1B	BAF250B, DAN15, P250R
ARID2	BAF200
SMARCD1	BAF60A, CRACD1, RSC6P
SMARCD2	BAF60B, CRACD2, RSC6p, SGD2
SMARCD3	BAF60C, CRACD3, RSC6P
PHF10	BAF45A, XAP135
DPF1	BAF45B, NEUD4, NeuroD4
DPF2	BAF45D, UBID4, REQ
DPF3	BAF45C, CERD4, FLJ14079
SMARCC1	BAF155, CRACC1, RSC8, SRG3, SWI3
SMARCC2	BAF170, CRACC2, RSC8
ACTB	BRWS1
ACTL6A	BAF53A, ACTL6, ARP4, INO80K
ACTL6B	BAF53B
SMARCB1	BAF47, SNF5L1, SNF5, INI1
SMARCE1	BAF57, CSS5
BCL7A	
BCL7B	
BCL7C	
BCL11A	ZNF856, CTIP1, EVI9
BCL11B	ZNF856B, CTIP2
SS18	SSXT, SYT
SS18L1	CREST, KIAA0693
BRD4	HUNK1, HUNKI, (M)CAP
BICRA	GLTSCR1
BICRAL	GLTSCR1L